Particle Accelerators, Vol. 62, pp. 139–163
Reprints available directly from the publisher
Photocopying permitted by license only

ELECTRON MULTIPACTOR CODE FOR HIGH-POWER RF WINDOW DEVELOPMENT

STANLEY HUMPHRIES JR*

Department of Electrical and Computer Engineering, Room 110, EECE Building, University of New Mexico, Albuquerque, NM 87131, USA

(Received 1 December 1997; Revised 9 February 1998; In final form 20 February 1998)

This paper discusses preliminary results from a versatile simulation code for charged-particle orbits under the combined influence of electrostatic, magnetostatic and electromagnetic fields. The finite-element program was developed to study electron multipacting in high-power accelerators under development for the production of tritium. For this application, the program can handle electron surface interactions with materials that have energy-dependent secondary emission coefficients. Calculations for three applications are described. A search for multipacting conditions in superconducting cavities for high-power proton beams gave a null result. In contrast, the code showed a strong possibility of electron multipacting in coaxial transmission lines that transmit power to the cavities. The application of weak static electric and magnetic fields could alleviate this problem. Studies of a coaxial vacuum window assembly showed that the growth of electron density in the downstream transmission line could contribute to breakdown. Distortions of electromagnetic fields near the feedthrough cause an upstream drift of electrons to the window surface.

Keywords: Electromagnetic simulations; RF breakdown

1. INTRODUCTION

This paper describes electron multipactor[1,2] simulations with the code Trak_RF. The integrated finite-element software system follows charged-particle trajectories in combined electrostatic, magnetostatic and electromagnetic fields. The program was developed to investigate

* Tel.: 505-296-6689. Fax: 505-294-0222. E-Mail: humphrie@warlock.eece.unm.edu.

possible contributions of electron multipacting to vacuum breakdown of RF (radio-frequency) windows for high-power accelerators. The studies support a cooperative program on Accelerator Production of Tritium (APT) at Los Alamos National Laboratory and the Savannah River Site.[3] The program goal is a continuously operating proton linac that generates a 1.3 GeV beam with an average current of 100 mA, equivalent to 130 MW. The accelerator demands powerful RF systems with high reliability. The possibility of vacuum window breakdown is a critical concern. To address the issue, an experimental and theoretical program of window testing and development has been initiated at Los Alamos.[4] The University of New Mexico supports this effort through the development of particle and radiation diagnostics to warn of impending breakdowns and computer codes to model the dynamics of stray electrons near windows.[5]

The first part of the paper reviews computational methods and capabilities of Trak_RF. The second part describes multipactor studies for APT prototype cavities and a 350 MHz coaxial vacuum window. Section 2 describes field calculation techniques used in the program with emphasis on frequency-domain electromagnetic solutions. The electromagnetic solver handles open and closed systems with frequency-dependent material losses and absorbing boundaries of any shape. Section 3 covers particle orbit calculations that use independent solutions for static and dynamic fields. Trak_RF has several features to model electron multiplication through secondary emission. Section 4 covers RF field calculations and electron multipactor studies for the superconducting cavities of the APT accelerator. Section 5 addresses electron multipacting in uniform coaxial transmission lines over a range of transmitted power. The calculations show how applied magnetic and electrostatic fields can shift or suppress multipactor bands. The final section describes simulations of electron histories near an alumina vacuum window in a coaxial line. Field perturbations near the assembly cause an upstream drift of electrons to the window surface. Multipacting in the downstream transmission line combined with the drift suggests a possible window breakdown mechanism. The results give insight on the placement of early warning detectors and suggest optimal locations for coatings to reduce secondary emission. The simulations also show that weak magnetic and electrostatic fields may prevent both multipacting and electron migration.

2. FIELD CALCULATIONS IN TRAK_RF

All static and dynamic field calculations in Trak_RF are carried out on conformal meshes.[6] Figure 1(a) shows a mesh to calculate transverse-electromagnetic wave propagation through a coaxial vacuum window. The elements are triangles that are flexed so that sides lie along material boundaries. Each element has an assigned region number. A region consists of a group of contiguous elements with a material identity. In the example, the regions represent the surfaces of metal conductors, the intervening vacuum, an alumina window and a resistive layer for wave absorption. An advantage of an element-based approach is that each triangle is uniquely associated with material properties. In electron multipactor calculations this property allows accurate characterization of particle collisions with surfaces. Finite-element field calculations on conformal meshes[7–9] have other advantages: accurate field evaluation near shaped surfaces, correct representation of field discontinuities at dielectric and ferrite boundaries, and easy implementation of the Neumann condition on angled and curved boundaries. Trak_RF uses the standard mesh

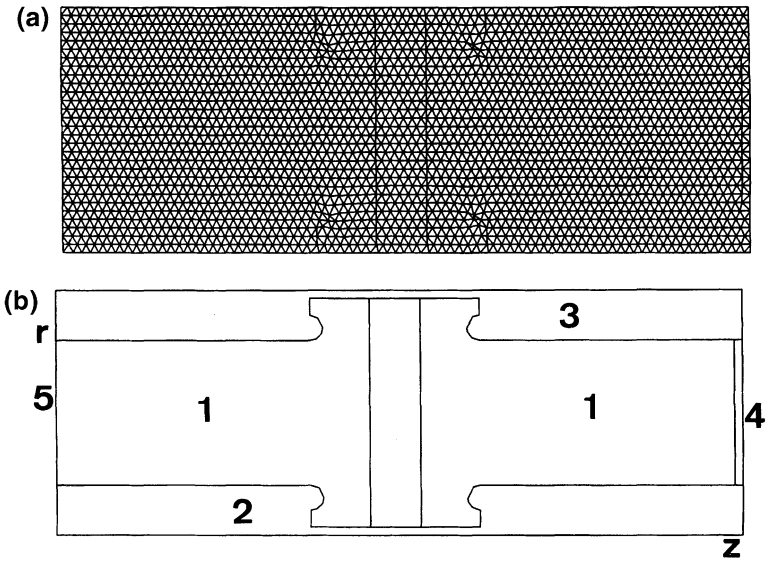

FIGURE 1(a) and (b)

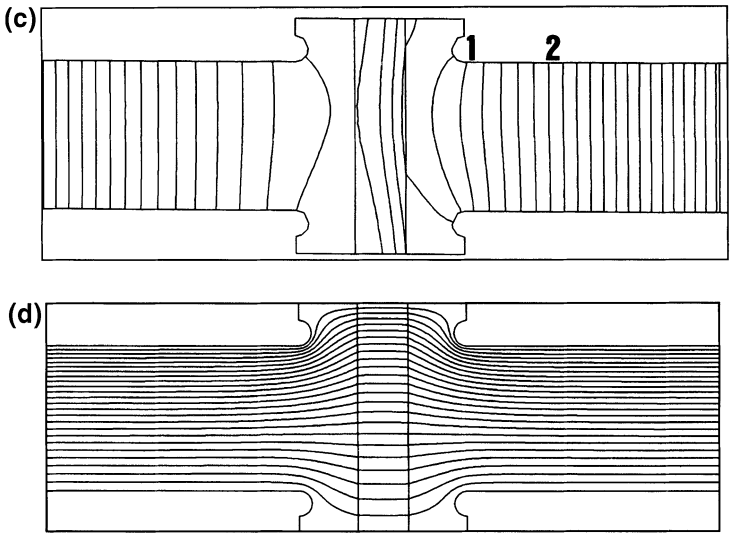

FIGURE 1(c) and (d)

FIGURE 1 High-power coaxial RF window assembly. (a) Conformal triangular mesh for finite-element calculations of electromagnetic and electrostatic fields. (b) Assembly geometry. Dimensions: $r_{min} = 0.70''$, $r_{max} = 3.60''$, $z_{min} = -4.00$, $z_{max} = 4.10''$. Region 1: vacuum. Region 2: inner metal wall. Region 3: outer metal wall. Region 4: matched termination layer. Region 5: drive boundary to initiate TEM wave. (c) Contours of the real part of rH_θ at $t = 0.0$ for the electromagnetic solution. The lines are parallel to lines of the real part of the electric field. Numbers show emission locations for orbits in Figure 12. (d) Equipotential contours for the electrostatic solution (normal to electric field lines).

generator and field solvers of the TriComp system.[10] Boundary information is entered through an interactive drafting program or from CAD software. The basic electrostatic and magnetostatic programs use a linear finite-element formulation[11,12] with solutions by successive over-relaxation.

The method used for electromagnetic field solutions is described in Ref. [6]. As an illustration, consider the equations for a planar structure (no variation in z) with electric field polarization E_z. The governing differential equation for an E-type solution is

$$-\nabla \times \left(\frac{1}{\mu}\nabla \times E_z z\right) = -\epsilon\omega^2 E_z z + \mathrm{j}\omega J_{oz} z. \tag{1}$$

The quantities μ and ϵ in Eq. (1) may have imaginary parts to represent losses from resistivity or non-ideal material reponse. The current

source J_{oz} contains information on the amplitude and phase of drive regions. Figure 2 shows the geometry and indices of vertices and elements surrounding a test vertex. In the example, the mesh has a regular logic with six elements encompassing each vertex. The finite-element equation for wave propagation at the test vertex is determined by taking area integrals of Eq. (1) over the surface surrounded by the dashed line in Figure 2. The result is

$$E_{zo}\left(-\sum_i W_i + \omega^2 \sum_i \frac{\epsilon_i a_i}{3}\right) + \sum_i E_{zi} = \mathrm{j}\omega \sum_i \frac{J_{iz} a_i}{3}. \tag{2}$$

The index i refers to the vertices surrounding the test vertex marked o. The quantities E_{zi} are complex numbers to represent field amplitude and phase. The quantities ϵ_i, μ_i and J_{iz} are the material properties and current density of the elements. The coupling coefficients are given by

$$W_i = \frac{\cot\theta_{bi+1}/\mu_{i+1} + \cot\theta_{ai}/\mu_i}{2}. \tag{3}$$

Equation (2) represents a large set of coupled linear equations, one for each mesh vertex. The set is solved in Trak_RF using matrix

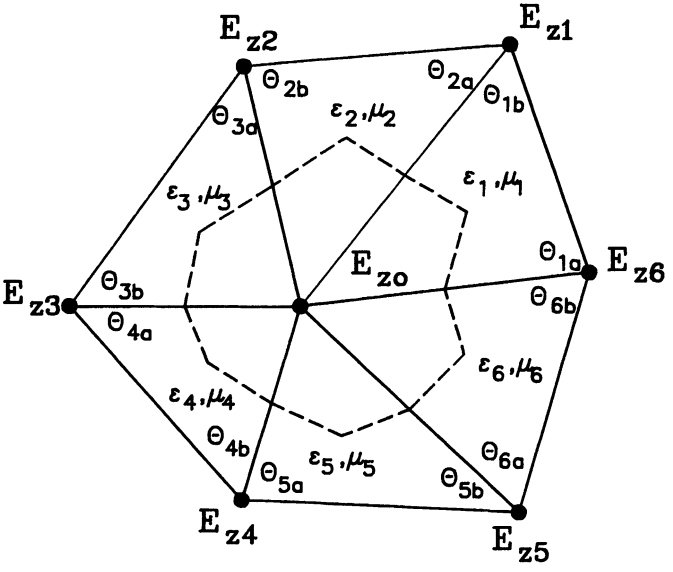

FIGURE 2 Mesh conventions for finite-element electromagnetic solutions, E-type waves in planar geometry. Dashed line is an integration path to derive Eq. (2).

inversion by block decomposition. The complex values E_{zi} give the physical electric field at a given RF phase. Numerical derivatives give the magnetic field components B_{xi} and B_{yi} in elements. In resonant solutions in closed regions, current sources act as coupling loops to create electromagnetic fields. The field solver also handles scattering in open systems. In this case, a convenient way to initiate fields is with a drive boundary with a fixed value of complex electric field amplitude. In solutions with E_z polarization, the Dirichlet condition $E_z = [0, 0]$ represents a metal wall. For H_z polarization (H-type waves), a metal surface is represented by an open-circuit boundary (Neumann condition). In scattering problems, an important advantage of the finite-element method is the use of termination layers of arbitrary shape to represent free-space boundary conditions.[6] The procedure is to set up a thin layer of width Δ on the outside of the solution volume. For E-type solutions, the imaginary part of the dielectric constant in the layer is assigned the value $\epsilon'' = -\sigma/\omega$. The conductivity σ is matched to the impedance of the adjacent medium,

$$\sqrt{\frac{\mu}{\epsilon}} = \frac{1}{\sigma\Delta}. \tag{4}$$

The performance of absorbing layers equals or exceeds that of look-back techniques.[13] For moderate mesh resolution the reflected energy from a termination layer is typically less than 1 part in 10^5.

3. CHARGED-PARTICLE ORBIT CALCULATIONS

Charged-particle orbit calculations in Trak_RF are straightforward. They involve Runge–Kutta integrations for up to 1000 particles using numerically calculated field components. Independent orbit calculations are performed for each particle, so the code applies to the early stages of multipacting before space-charge effects are important. The main challenge is organizing the broad range of possibilities. The program can handle three numerical field solutions on independent conformal meshes: electrostatic, magnetostatic and electromagnetic. Field geometries can be mixed in any combination. The two-dimensional quasi-static solutions may be planar or cylindrical. There are four

possibilities for electromagnetic fields: planar geometries with primary field components E_z or H_z or cylindrical systems with solutions for rE_θ or rH_θ. Trak_RF uses a reference three-dimensional Cartesian coordinate system. Translations and rotations within this system can be applied to the field solutions. During orbit tracking, the program performs interpolations on all field solutions to derive total values of **E** and **B** at the position and elapsed lifetime of the particle. The standard method to initiate particle orbits is through a parameter listing file that can be generated by spreadsheets or user-written programs. The file specifies charge, mass, initial kinetic energy, position and direction cosines. A reference phase can be assigned when electromagnetic fields are present. The program can also generate a variety of particle distributions. Working from user-supplied numerical tables, Trak_RF can set up arbitrary distributions in energy, position and direction. The program has several options to stop orbits, including maximum distance and elapsed time. It is also possible to set up stopping planes along the reference axes for high-accuracy interpolations of crossing particle parameters.

Trak_RF has special features for electron multipacting. In this application, an orbit represents the history of a group of electrons. Orbits are initially assigned a multiplication factor of 1.00. The fate of a group depends on interaction with material elements as the model electron moves under the influence of fields. In this application the mesh regions for the static and dynamic field solutions are assigned one of three characteristics: *Vacuum*, *Material* or *Secondary*. At each integration time step, Trak_RF checks the status of the element that contains the orbit. For a *Vacuum* element the particle continues unimpeded. An orbit is terminated if it enters a *Material* element or leaves the field solution volume. The sequence of events for a *Secondary* element is more involved. The particle is restored to its position before entering the surface and assigned a low momentum in the opposite direction. The particle multiplication factor is multiplied by the secondary-emission coefficient of the material, δ. This quantity equals the number of low-energy electrons emitted per electron incident on a surface. If the particle immediately reenters the material, then the collision occurred during the decelerating phase of the electromagnetic field. In this case the orbit is terminated. Orbits that reach the end of their lifetime with multiplication factors much larger

than unity signal the possibility of multipacting. This result occurs only if the orbit makes many strikes on secondary surfaces at the correct phase of the electromagnetic field with the condition $\delta > 1$.

The secondary-emission coefficient depends strongly on the incident electron kinetic energy T_e. For clean metal surfaces, δ exceeds unity over electron kinetic energies in the range 100 eV to 1 keV. Low-energy electrons do not deposit enough energy to eject secondaries, while high-energy electrons penetrate below the critical surface layer. Values of δ may be considerably higher for contaminated surfaces. Trak_RF can handle any variation of $\delta(T_e)$ through the use of tabular functions, user-supplied tables of δ versus T_e in ASCII format. A run can include up to 10 tables of 256 entry pairs to represent different materials. Up to 127 *Secondary* regions can be associated with the tables. Trak_RF uses the electron kinetic energy at the point of entry into the *Secondary* element to determine δ by either linear or cubic spline interpolation. Reference [14] lists secondary-emission parameters for a variety of materials. The tables give the maximum value of δ, the corresponding value of T_e, and the kinetic energy range where $\delta > 1$. Tables of $\delta(T_e)$ in Trak_RF format have been generated for common metals by fitting the parameters with a second-order function that goes to zero at $T_e = 0$ and drops a $1/T_e^{1/2}$ at high energy. Figure 3 shows a plot of tabular values for the table *niobium.sec* used in the calculations of this paper. The secondary-emission coefficient also depends on the electron angle of incidence, θ. The theoretical dependence is $\delta_\theta = \delta \,\text{secant}(\theta)$, where δ is the value at normal incidence. The relationship implies strong enhancement for grazing-incidence electrons. Because Trak_RF handles emission surfaces of arbitrary shape, the present version does not include angular corrections. These effects may be important in simulations of resonant cavities; therefore, we are adding routines to identify local surface orientation for comparison with the incident electron trajectory to yield δ.

Trak_RF includes standard diagnostics of the Trak gun design code.[15] These include orbit listings and plot files that can be analyzed with an interactive graphics utility. There are several additional diagnostics for the multipactor process. The program lists the multiplication factor, the number of strikes in secondary emission elements, the elapsed time and the total distance traversed by each orbit. The

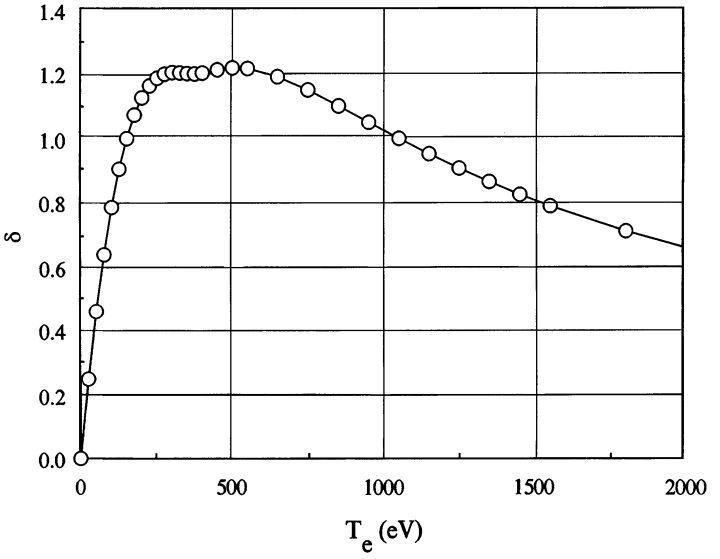

FIGURE 3 Data points to define $\delta(T_e)$, the energy-dependent secondary emission coefficient for niobium in Trak_RF runs.

average multipactor order equals the elapsed time divided by the product of number of strikes times the RF period. The program also calculates a global multiplication factor equal to the total number of electrons at the end of the calculation (given by the sum of individual multiplication factors) divided by the number of initial orbits. Another useful diagnostic is the number of wall strikes organized by mesh region. This information helps pinpoint the locations of secondary emission or particle loss. Trak_RF creates tables of initial and final orbit parameters including position, kinetic energy, total travel distance and elapsed time. Information on net displacement must be combined with the multiplication factor to judge if self-sustained multipacting is possible.

4. APT CAVITY MULTIPACTOR SIMULATIONS

The main section of the APT linear accelerator will consist of coupled arrays of superconducting cavities operating at 700 MHz.[16] The present design calls for five-cell arrays operating in the π mode (the

RF phase difference between adjacent cavities equals 180°). Although there is considerable operational experience with superconducting electron accelerators, the application to high-power proton beams is novel. The requirement for synchronization of non-relativistic particles leads to modified cavity geometries. Furthermore, the cavity length must vary through the machine to match the changing proton velocity, v_z. For a given value of the velocity factor $\beta = v_z/c$, the effective cavity length L is constrained by the synchronization condition $L = \beta c/2f$.

The electromagnetic field solution component of Trak_RF was tested in benchmark resonant mode searches of the arrays described in Ref. [16]. Figure 4 shows the geometry and finite-element mesh for $\beta = 0.64$. The cavity walls have an open-circuit boundary condition for the H-type accelerating modes. The computation used approximately 15,000 elements to model half of the assembly with a symmetry boundary at the midplane. The symmetry limited the number of oscillations to three with phase differences of 0°, 90° and 180°. The RF modes were excited by a capacitive coupler near the axis with an oscillating axial current at 0° phase. The cavity response was detected by a magnetic field probe near the outer radius of the central cavity. An initial calculation was performed with the scan mode of the field solver. In this mode the program makes linear or logarithmic frequency scans with listings of the real and imaginary parts of rH_θ at the probe position. For H-type waves, a resonance corresponds to a negative-going zero transition of the real part of rH_θ. In systems with loss, the cavity Q factor can be determined from the shape of the imaginary part of rH_θ near resonance. The plot of Figure 5 shows the variation of the real part of the probe reponse with the positions of the three resonant modes. Once the range is identified, the field solver can lock onto the resonance using a Winjgaarden–Dekker–Brent[17] search to identify the probe zero crossing. The frequency predictions are 682.60 MHz for the 0 mode, 694.09 MHz for the $\pi/2$ mode and 701.62 MHz for the desired π mode. The latter value is close to results from Mafia[18] and Superfish.[19]

Multipactor calculations were performed for the APT single-cell test cavities. The results are encouraging, but should be interpreted with caution because the present version of the Trak_RF does not locate the multipacting bands reported in Refs. [20–22] for coupled

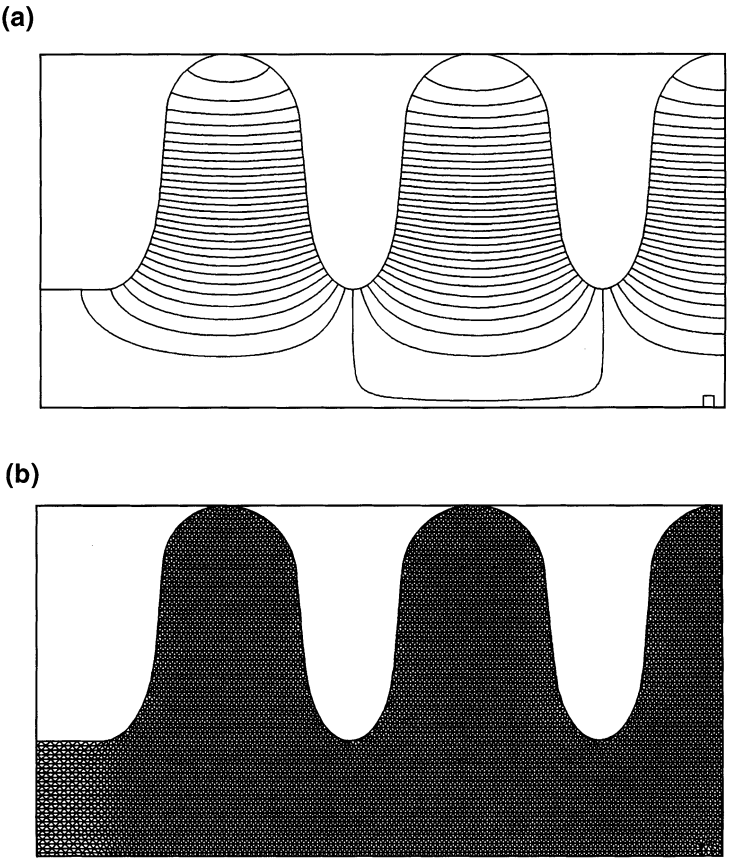

FIGURE 4 Resonant mode calculations for the APT cavity arrays at $\beta = 0.64$. Dimensions: $r_{min} = 0.0$ cm, $r_{max} = 19.4$ cm, $z_{min} = -38.0$, $z_{max} = 0.0$ cm. (a) Geometry of a half array with a symmetry boundary on the right. Beam pipe to the left not shown. Small box on axis is the capacitive drive. Contours of rH_θ show electric field lines for the π mode. (b) Conformal variable resolution mesh with 15,000 vertices.

cavities with flat equators. These references describe numerical calculations that are in good agreement with experimental observations. It is probable that the discrepancy results from the absence of incident-angle corrections in Trak_RF which may be substantial in the outer cavity regions where RF magnetic fields are relatively strong. Figure 6 shows the geometry of the $\beta = 0.48$ prototype cavity. Region 1 represents a block of niobium. This region is treated as an ideal void for

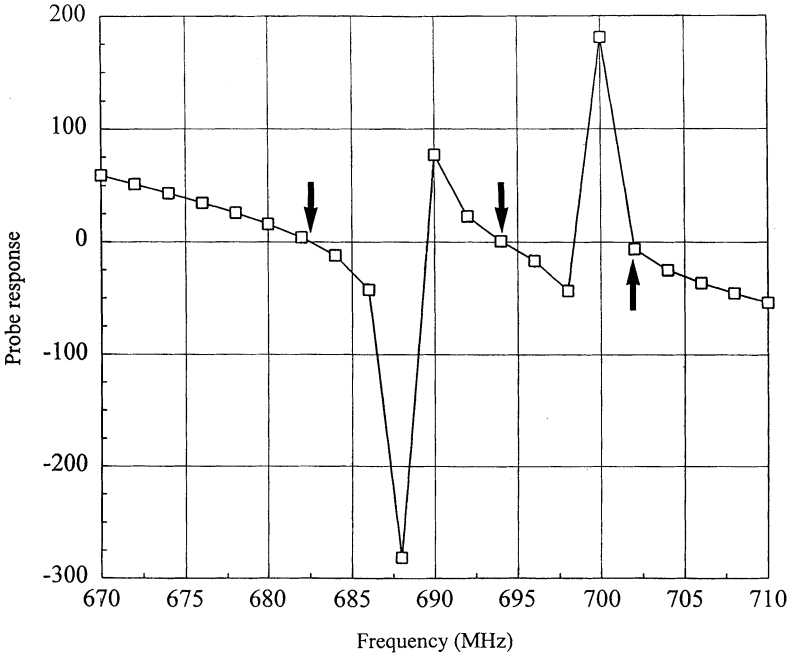

FIGURE 5 Probe response, cavity array of Figure 4. Plot of $\mathrm{Re}(rH_\theta)$ near the equator of the central cavity as a function of frequency. Arrows indicate resonance conditions for the 0, $\pi/2$ and π modes.

the RF field calculation, giving an open-circuit condition on the cavity boundary. In the orbit calculation, Region 1 is a *Secondary* material with $\delta(T_e)$ given by the data of Figure 3. Region 2 is the vacuum volume of the cavity carved out of Region 1. Region 3, with vacuum material properties and an axial current density, drives the TM_{010} mode. The simulation also included 20 cm end pipes that are not shown in Figure 5. A mode search gives a resonant frequency of 698.99 MHz.

Electron orbits were initiated near the cavity equator at the five sites shown as filled circles in Figure 6. Nineteen orbits were created at each position at 10° intervals over the RF phase range for acceleration away from the wall. To compare the results to experiments the calculations were parametrized in terms of the peak electric field stress on the cavity wall (marked with an open circle in Figure 6).

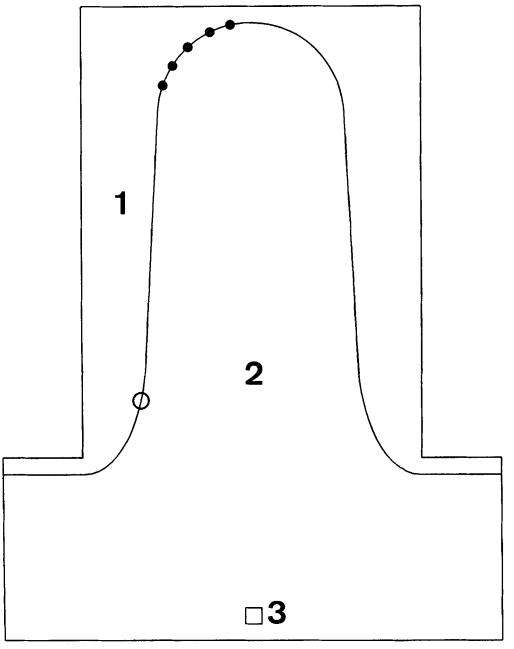

FIGURE 6 Geometry for multipactor calculations. APT $\beta = 0.48$ single-cell test cavity at 700 MHz. Dimensions: $r_{min} = 0.0$ cm, $r_{max} = 19.1$ cm, $z_{min} = -7.5$ cm, $z_{max} = 7.5$ cm. Region 1: niobium wall. Region 2: vacuum. Region 3: capacitive drive. Filled circles show the emission points of model electrons. Open circle shows the point of maximum electric field.

The range from 2 to 50 MV/m was covered in increments of 2 MV/m. Trak_RF showed no conditions for either the global growth of electron density or high multiplication factors for individual orbits. For isolated conditions some particle orbits had multiple wall strikes but did not achieve high multiplication factors. Figure 7 shows an example for an electron emitted at a field of 40 MV/m from the position in Figure 6 closest to the equation. The orbit exhibits two-point multipacting with 16 wall collisions each half RF period. The orbit migrates to the cavity equator where its kinetic energy drops below the level for electron multipication, in agreement with the results of Ref. 21 for toroidal cavities. I found similar results for test cavities at $\beta = 0.64$ and 0.82. The absence of multipacting agrees with on-going experiments at Los Alamos National Laboratory.[23]

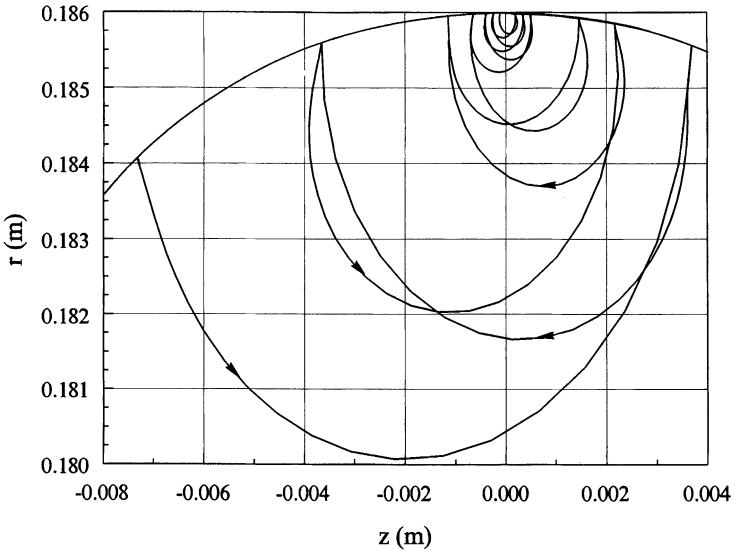

FIGURE 7 Small-scale orbit of an electron emitted near the equator of the cavity of Figure 6 at a peak field of 40 MV/m.

5. ELECTRON MULTIPACTOR CALCULATIONS FOR COAXIAL TRANSMISSION LINES

Multipactor calculations are easier to perform in non-resonant structures like RF feedthroughs. At typical field levels electrons in the keV range have large-scale orbits with approximately normal incidence on surfaces and exhibit multipacting over broad power bands. Calculations were performed for the coaxial transmission line shown in Figure 8(a). The dimensions are the same as the coaxial window assembly described in the next section that will be used in the low-frequency section of the APT accelerator. The inner radius of 1.3″ (0.03302 m) and outer radius of 3.0″ (0.07620 m) gives a characteristic impedance of 50.22 Ω. The figure illustrates a method to set up a TEM (transverse electromagnetic wave) solution in the transmission line. The primary field quantity for H-type waves in the cylindrical assembly, rH_θ, is given by an equation similar to Eq. (2). Region 1 is vacuum with $\epsilon = \epsilon_o$ and $\mu = \mu_o$. The solution volume length of 8.0″ is sufficient to contain drifting electrons in the orbit calculation. Region 2 is a single layer of elements on the inner boundary that assumes secondary emission

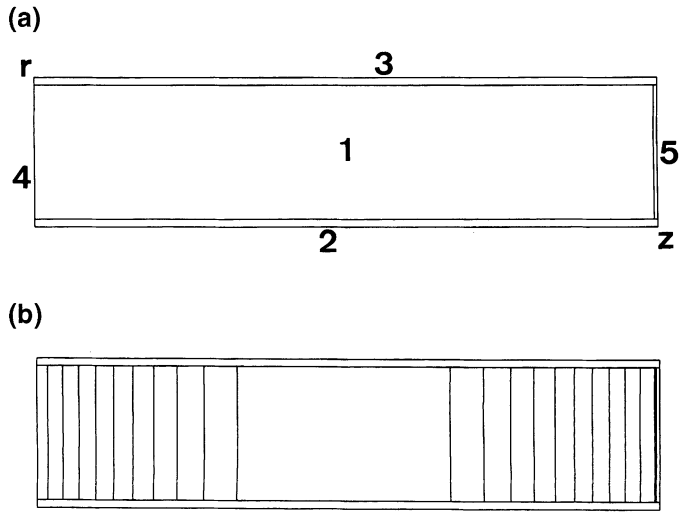

FIGURE 8 Multipactor calculations for a high power transmission line – electromagnetic field solutions. Dimensions: $r_{min} = 1.20''$, $r_{max} = 3.10''$, $z_{min} = -4.00''$, $z_{max} = 4.05''$. (a) Geometry. Region 1: vacuum. Region 2: inner conductor. Region 3: outer conductor. Region 4: drive boundary, phased to give peak real part of E_r at $z = 0.0$ and $t = 0.0$. Region 5: matched termination layer. (b) Contours of $\mathrm{Re}(rH_\theta)$, showing $E_r(z, 0)$ for the 350 MHz TEM wave.

properties for the orbit calculation. For the electromagnetic solution these elements have infinite impedance, defining an open-circuit boundary at the surfaces of the vacuum region. Region 3 at the outer boundary has similar properties. Region 4 is a drive boundary the specified field value

$$rH_\theta = 1.004 \cos(2\pi ft + 0.265\pi), \quad \text{(A)} \tag{5}$$

where $f = 350$ MHz. The choice of amplitude gives a time-averaged wave energy of 1 kW. In the orbit calculation, the field values are multiplied by an adjustment factor to cover a range of power. The target operating level for the vacuum window of Section 6 is 700 kW. The phase offset of 42.67° ensures that the radial electric field has a maximum positive value at the line midplane when $t = 0$. Finally, Region 5 is a termination layer[24] that acts as an ideal absorber. In contrast to absorbing boundary techniques[25] which demand multiple element layers with carefully programed properties, the termination method requires only a single layer. Furthermore, it approaches ideal

performance in the limit of zero thickness. In the simulation of Figure 8, the layer of thickness 0.05″ (1.27×10^{-3} m) is matched to the characteristic impedance of vacuum when $\epsilon = \epsilon_0$ and $\mu = \mu_0$ (1.0–104.23j). Figure 8(b) plots contours of the real part of rH_θ which lie along electric field lines.

In the orbit calculations electrons were initiated near the inner and outer metal surfaces. The secondary regions were assigned the properties of niobium (Figure 3) which characterize a broad class of materials including copper and iron. At all power levels, multiplication occurred only for orbits that started on the outer wall. Inner wall orbits that achieved high multiplication factors invariably had crossed the gap and created secondaries on the outer wall. Orbits terminated if they met one of the following conditions: (1) striking a surface during the decelerating phase, (2) moving axially out of solution space, (3) having a multiplication factor below the minimum level (10^{-4}), or (4) having a lifetime exceeding the maximum run time. The time limit in the simulations was 250 ns, equal to 87.5 RF periods. Taking $\delta_{max} = 1.3$, the maximum possible multiplication factors were 9.33×10^9 (first-order multipacting), 9.7×10^4 (second-order), 2.1×10^3 (third-order) and 3.1×10^2 (fourth-order). Electron multiplication was calculated over a range of average transmitted power from 100 to 1000 kW. In the baseline run, electrons were initiated at $z = 0.0$ on the outer wall in 10° intervals over the RF phase for inward acceleration (−90° to 90°).

Figure 9 shows the resulting global multiplication factor as a function of transmitted power. There are strong bands at 210, 290, 420 and 690 kW corresponding to different multipactor orders which could be important during the RF start-up phase. Electron multiplication was limited mainly by the run time; therefore, the difference in amplitude gives a rough idea of the electron density growth rate. The 690 kW band is the one of prime concern since it overlaps the projected operating level in the APT accelerator. In this band, there was strong multiplication for electrons emitted over the phase range −90° to 20°. These orbits followed a downstream drift motion in the traveling wave. The net displacements were relatively small; therefore, the growth of local electron density was possible. The average axial displacement was 2.5″ compared to an integrated pathlength of about 100″. Similar results hold for the other bands. High multiplication

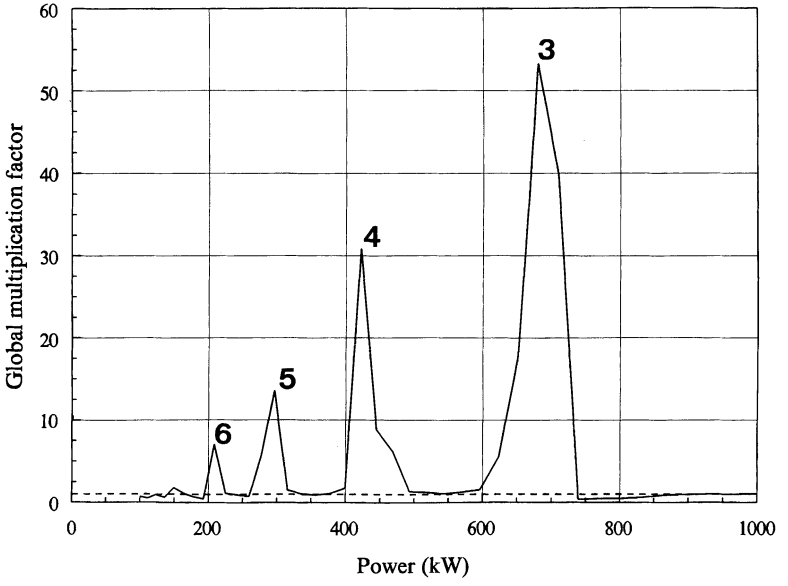

FIGURE 9 Electron multipactor simulation for the transmission line of Figure 8 with no static fields. Plot of global multiplication factor as a function of average transmitted power. Numbers indicate the order of single-point multipacting.

factors were associated with electrons in the phase range $-90°$ to $20°$ and the downstream drifts ranged from $1.0''$ to $1.7''$. Figure 10 shows plots of $r(t)$ for electrons emitted at a phase of $-45°$ in the third, fourth and fifth order multipactor bands. The numerical integrations had good accuracy. Second-order field interpolations were applied over an element size approximately 5 per cent of the orbit scale size.

Several options were investigated to reduce electron multipacting. The simplest was a change in the transmission line geometry. Electron multiplication dropped as the size of the line increased. For example a 50 per cent increase in the radii of the inner and outer conductors eliminated multipacting over the full power range except for a narrow band of order 7–8 at 800 kW. These electrons attained a maximum multiplication factor of only 5.8 in 250 ns with an axial displacement of $2''$. Another approach to modify multipacting is the application of magnetic fields. These fields significantly affect the orbits of electrons when the parameter ω/ω_g is on the order of unity or higher. Here ω is the RF angular frequency and ω_g is the electron gyrofrequency

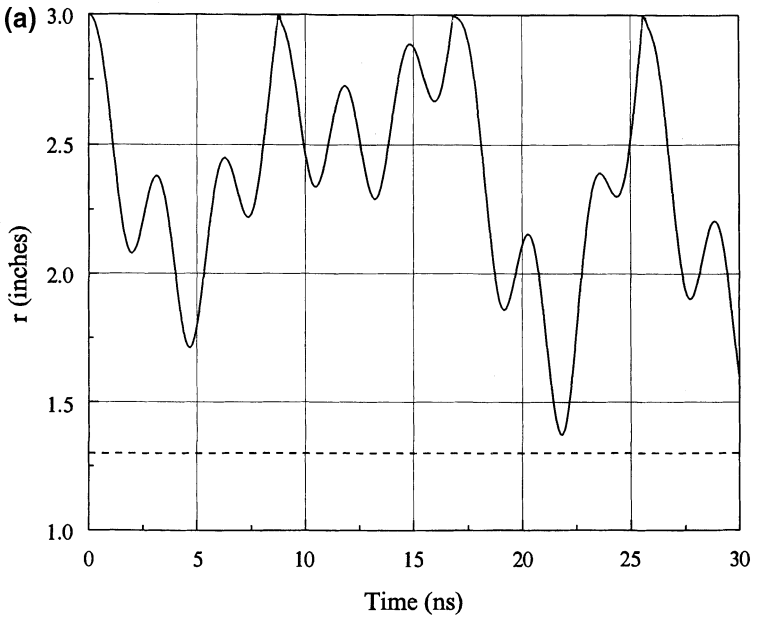

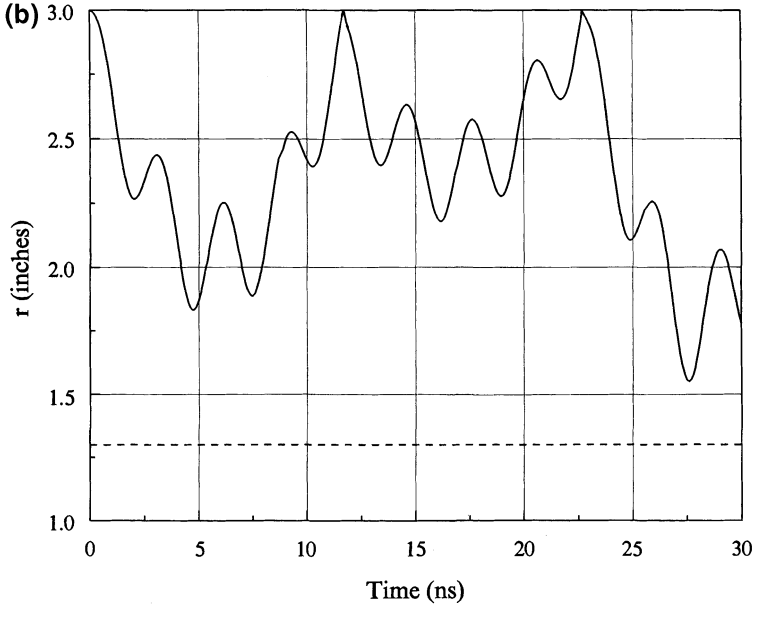

FIGURE 10(a) and (b)

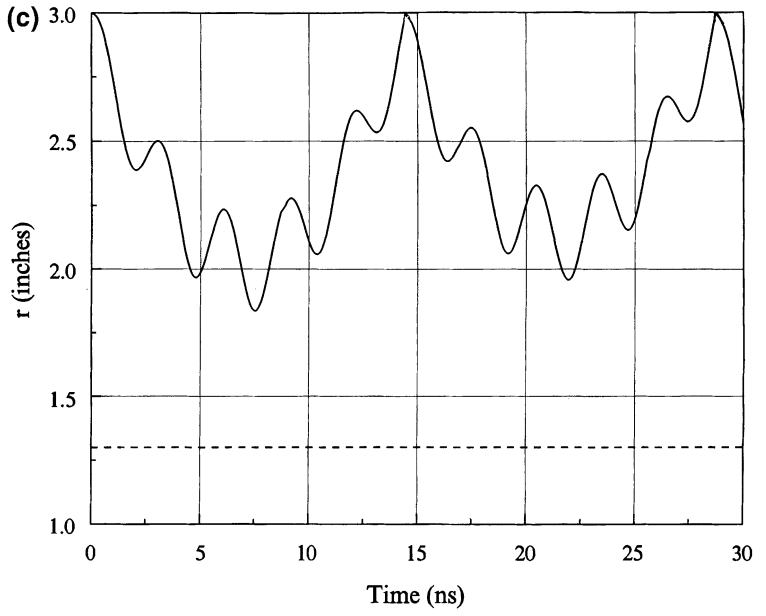

FIGURE 10(c)

FIGURE 10 Calculated electron history orbits $r(t)$ for the solution of Figure 8. Initial electron emission from outer wall at a phase of $-45°$. Dashed line corresponds to inner conductor. (a) Third order single-point multipactor, 680 kW. (b) Fourth-order, 420 kW. (c) Fifth-order, 290 kW.

(related to the applied field B_o by $\omega_o = eB_o/m_e$). Initial simulations with a uniform axial field, $B_o\mathbf{z}$ showed that weak fields ($\omega_g/\omega \ll 1$) shifted multipactor bands to lower power levels. Figure 11(a) illustrates the effect. The plot shows the global multiplication factor over the power range of interest for $\omega_g/\omega = 0.00$, 0.05 and 0.10 (corresponding to $B_o = 0.0$, 6.25 and 12.50 G at $f = 350$ MHz). As an example, a 6.25 G axial field shifted the peak of the third-order multipactor band from 680 to 570 kW. In some cases, the shifts worsened multipactor effects. For example, at $\omega_g/\omega = 0.10$ a strong second-order band shifted to overlap the 700 kW operating level. High fields give stronger shifts. Figure 11(b) plots multiplication factor plots for $\omega_g/\omega = 0.20$ and 0.50 ($B_o = 25.00$ and 62.5 G). At the larger value, the first-order band shifted to the lower end of the power range. Higher fields gave complete suppression of multipacting.

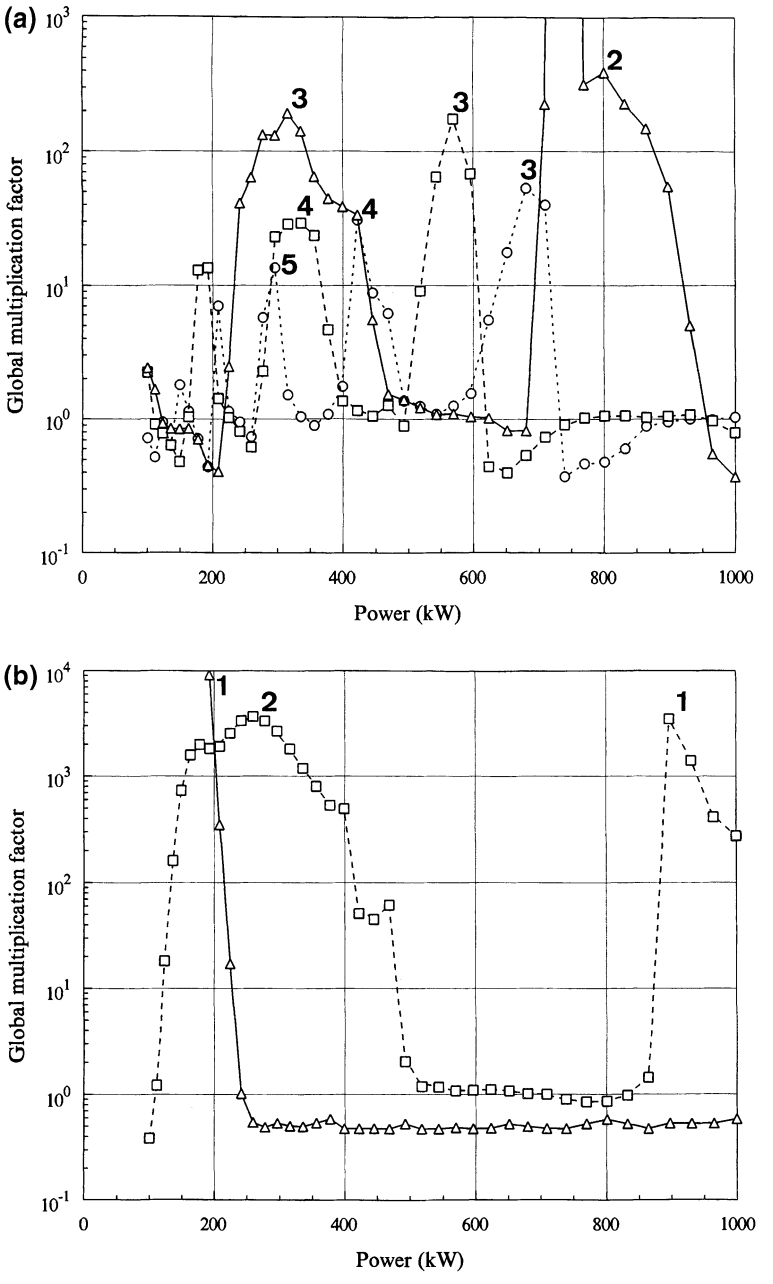

FIGURE 11 Effect of axial magnetic field on multipacting in the transmission line of Figure 8. Global multiplication factor versus transmitted power. Numbers above peaks show multipacting order. (a) Weak field. Open circles: $\omega/\omega_g = 0.00$. Open squares: $\omega/\omega_g = 0.05$. Open triangles: $\omega/\omega_g = 0.10$. (b) Moderate field. Open squares: $\omega/\omega_g = 0.20$. Open triangles: $\omega/\omega_g = 0.50$.

Transverse magnetic fields (B_x, B_y) also influence multipacting. In the case, the orbit history depends on the azimuthal location of emission. Suppose the baseline emission site is $x=0.0$, $y=r_o$ and $z=0.0$. For this choice, the field $B_o\mathbf{y}$ is parallel to the electric field at the emission point. For this geometry the applied field had a negligible effect on multiplication factors although it impeded axial electron migration. A field $B_o\mathbf{x}$ normal to E_r at the emission site significantly reduced electron multipacting. An applied field of only a few Gauss eliminated multiplication for electrons emitted in the y–z plane in the over the full transmitted power range.

Application of an electrostatic field is a simple and effective method to eliminate multipacting. Electric fields can easily be applied in the coaxial vacuum window assembly of Section 6 by biasing the center conductor. This electrode can be supported by the window and capacitively coupled to upstream and downstream waveguides. To investigate the effect, a static electric field solution for the region between coaxial cylinders was combined with the RF field solution. At 700 kW, the peak RF electric field on the outer conductor is 1.32×10^5 V/m. A bias voltage of only 8.6 kV is sufficient to produce a static field with the same amplitude. Applied voltages much lower than this value were sufficient to eliminate multipacting over the full power range in the coaxial transmission line. With a voltage of 2.5 kV, the orbit lifetime at 700 kW extended over only 2–3 wall strikes. The static field quickly desynchronized electrons from RF field. For a positive bias most electrons struck the inner conductor. A negative bias also reduced or eliminated multipacting but for a different reason. Although orbits made up to 23 strikes on the outer wall, the number of electrons decreased because the strikes occurred at reduced kinetic energy.

6. ELECTRON MULTIPACTOR EFFECTS NEAR A HIGH-POWER RF WINDOW

Figure 1(b) shows the geometry of a generic high-power RF vacuum window of the type considered for the low-frequency section (350 MHz) of the APT accelerator. The space between the inner and outer conductors (marked as Region 1) has $\epsilon=\epsilon_o$ and $\mu=\mu_o$. The upstream volume represents a high pressure gas and the downstream volume is vacuum. Orbit calculations were performed in the vacuum

region. Region 2 is the inner conductor. Again, the elements are treated as voids for the field calculation and as secondary emission material for the orbit simulation. Region 3 is the outer conductor, Region 4 is an ideal absorbing layer, and Region 5 is a drive boundary. Far from the window the system constitutes 50.22 Ω coaxial transmission lines with the dimensions used in Section 5. The alumina window (Region 6) has $\epsilon = 7.8\epsilon_0$. The drive boundary is set to zero phase with amplitude of $rH_\theta = 1.0548$ A. This value produces a 1 kW traveling wave downstream with allowance for the 97 per cent transmission coefficient of the window assembly.

Figure 1(c) plots contours of rH_θ for the RF field solution at 350 MHz. Analysis of the real and imaginary parts of the solution gave the window transmission coefficient and the phase of the traveling wave in the vacuum region. Orbits were calculated at several downstream positions for 700 kW transmitted power. Following the results of Section 6, the electrons were emitted from the outer wall at a phase −45° relative to maximum positive value of the radial electric field. Electrons emitted near the window surface (distances to about 1.2″) were quickly accelerated into the window by the RF fields. Figure 12(a) shows the orbit of an electron generated at Point 1 of Figure 1(c). It reached the window surface with a kinetic energy of about 1 keV. It is unlikely that these electrons are a threat because they have no opportunity to multiply. Similarly, electrons generated far from the window (>2.2″) are not dangerous because they drift downstream under the influence of the traveling wave. The electrons of greatest concern are those created at an intermediate distance (1.2–2.2″). At certain power levels, these electrons exhibit strong multiplication with a gradual migration to the window. Figure 12(b) shows an orbit history for an electron created at Point 2 in Figure 1(c). This orbit made 15 wall strikes before accelerating into the window.

Simulations were also made to determine the effect of electrostatic fields. Figure 1(d) shows equipotential lines of the electrostatic solution. Runs were made for center conductor bias voltages of +2.5, +5.0 and −2.5 kV. Electrons were emitted from the outer wall at −45° phase at different axial positions. Orbit multiplication and axial migration was eliminated at all voltage levels. At +2.5 kV nearby orbits struck the window as in Figure 12(a). With an increase of

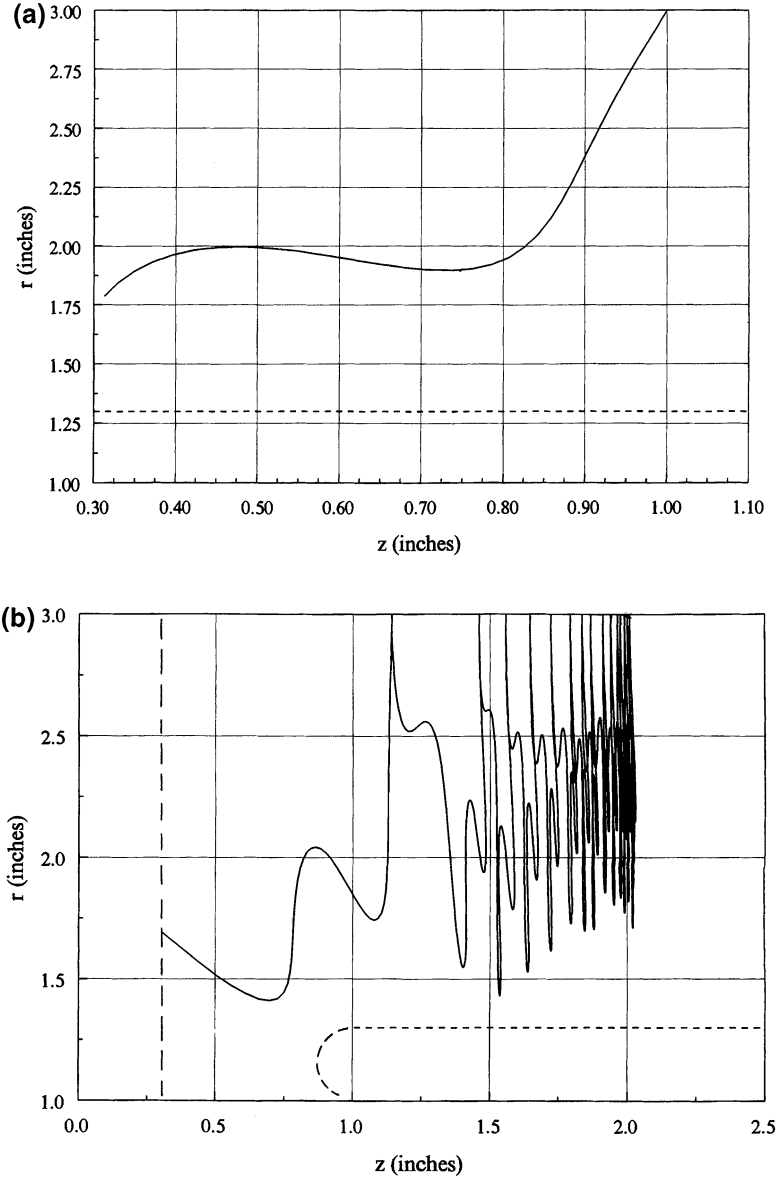

FIGURE 12 Orbits of electrons created near an RF vacuum window, 700 kW at 350 MHz. Window surface at $z = 0.030''$. (a) Electron initiated at Position 1 of Figure 1(c). (b) Electron initiated at Position 2 of Figure 1(c).

voltage to +5.0 kV, all electrons were absorbed on the inner conductor. Similarly, an applied voltage of −2.5 kV prevented migration to window surface by deflecting electrons back to the outer conductor. Therefore, a static bias field not only inhibited electron multiplication, but also reduced the chance that stray electrons would reach the window surface.

In conclusion, the results give an idea of potential danger areas and show where alternate suppression techniques might be effective. For example, wall coatings with low values of δ would probably be most effective if applied at distances of 1–2″ from the window surface. Similarly, if high-sensitivity electron detectors to warn of potential breakdown are feasible, they should be situated in this region. Presently, there is insufficient experimental evidence to judge the full significance of the simulations. Performance figures for commercial high-power RF windows are highly proprietary. Furthermore, window assemblies are extremely expensive so it is difficult to make detailed studies of breakdown conditions. Nonetheless, the calculations give some insight into effects that may occur and promising methods to reduce the probability of breakdowns. The work is continuing with studies of modified electrode shapes to repel electrons from the window assembly. The main task in future development of Trak_RF is to add routines to determine electron incidence angle for arbitrary resonator surface shapes. A three-dimensional RF code that can be applied to waveguide-type windows is under development. This program uses a unique time-domain finite-element approach with flexible mesh spacing and compatibility with termination layers. The mesh generator and field solver have been completed and tested. Particle tracking capabilities will be added in the next year.

This work was supported by the U.S. Department of Energy under Contract Number DE-FG04-97AL77993. I would like to thank Frank Krawczyk, Daniel Rees, Brian Rusnak and John Gahl for their valuable suggestions.

References

[1] A.J. Hatch, *Nucl. Instrum. and Methods* **41**, 261 (1966).
[2] See, for instance, S. Humphries Jr., *Principles of Charged Particle Acceleration* (Wiley, New York, 1986), Section 14.5.

[3] G. Lawrence *et al.*, *Conventional and superconducting RF Linac design for the APT Project, Proc. 1996 Int'l. Linear Acc. Conf.* (Geneva, 1996), to be published.
[4] D. Rees, P.J. Tallerico and M. Lynch, *IEEE Trans. Plasma Sci.* **25**, 1033 (1996).
[5] Private communication, J. Gahl, University of New Mexico.
[6] See, for instance, S. Humphries Jr., *Field Solutions on Computers* (CRC Press, Boca Raton, 1998).
[7] M.V. Chari and P.P. Silvester (eds.), *Finite Elements for Electrical and Magnetic Field Problems* (Wiley, New York, 1980).
[8] J. Jin, *The Finite-Element Method in Electromagnetics* (Wiley, New York, 1993).
[9] M.N. Sadiku, *Numerical Techniques in Electromagnetics* (CRC Press, Boca Raton, 1992).
[10] TriComp mesh generator and field solution programs courtesy of Field Precision, Albuquerque, New Mexico.
[11] P.E. Allaire, *Basics of the Finite Element Method* (W.C. Brown Publishers, Dubuque, 1985).
[12] J.L. Warren *et al.*, *Reference Manual for the Poisson/Superfish Group of Codes* (Los Alamos National Laboratory, LA-UR-87-126, 1987), unpublished.
[13] See, for instance, K.S. Kunz and R.J. Luebbers, *The Finite Difference Time-Domain Method for Electromagnetics* (CRC Press, Boca Raton, 1993), Chapter 18.
[14] D.R. Lide (ed.), *Handbook of Chemistry and Physics*, 74th Edition (CRC Press, Boca Raton, 1993), pp. 12–107.
[15] S. Humphries Jr., *J. Comp. Phys.* **125**, 488 (1996).
[16] F.L. Krawczyk, R.C. Gentzlinger, B. Haynes, D.I. Montoya, B. Rusnak and A.H. Shapiro, *Superconducting cavities for the APT accelerator, Proc. 1997 Particle Accelerator Conf.*, to be published.
[17] R.P. Brent, *Algorithms for Minimization Without Derivatives* (Prentice-Hall, Englewood Cliffs, NJ, 1973), Chapter 3.
[18] M. Bartsch *et al.*, *Computer Phys. Comm.* **72**, 22 (1992).
[19] K. Halbach and R.F. Holsinger, *Particle Acc.* **7**, 213 (1976).
[20] C.M. Lyneis, H.A. Schwettman and J.P. Turneaure, *Appl. Phys. Lett.* **31**, 541 (1977).
[21] G. Bienvenu, P. Fernandes and R. Parodi, *Nucl. Instrum. and Methods* **A320**, 1 (1992).
[22] P. Fernandes and R. Parodi, *NEWTRAJ, A Computer code for the simulation of the electron discharge in accelerating structures*, in: E.R. Lindstrom and L.S. Taylor (eds.), *Proc. 1987 Part. Acc. Conf.* (IEEE, Pascataway, NJ, 87CH2387-9), p. 1857.
[23] Private communication, F. Krawczyk, Los Alamos National Laboratory.
[24] S. Humphries Jr., *Finite-element solutions for electromagnetic scattering in inhomogeneous volumes, IEEE Trans Microwave Technology*, submitted.
[25] J.F. DeFord, *Investigation of the limitations of perfectly-matched absorber boundaries in antenna application*, in: E.C. Michelson (ed.), *Proc. Applied Computational Electromagnetics Conf.* (Naval Postgraduate School, Monterrey, CA, 1997), p. 592.